Optical tweezers and fluid characteristics of an optical rotator with slopes on the surface upon which light is incident and a cylindrical body

Hiroo Ukita and Kenji Nagatomi

The characteristics of the optical trapping force, optical torque, and viscous drag force for a newly proposed cylindrical optical rotator are analyzed. The optical trapping force and torque are evaluated by use of a ray optics model for both parallel and focused laser beam illumination. The drag force is calculated from computational fluid dynamics to be the sum of the components of both the pressure and the shearing stress on all the surfaces of the rotator. We analyze the rotation rate by balancing the optical torque with the drag force. A cylindrical optical rotator is expected to rotate at a high speed because of its highly efficient generation of optical torque and its small viscous drag force. © 2003 Optical Society of America

OCIS codes: 140.7010, 350.3950, 220.2740.

1. Introduction

An optical pressure rotator with an asymmetrical (shuttlecock) shape on one side has been proposed and experimentally demonstrated.[1] The torque exerted on the sidewall was analyzed by use of a ray optics model.[2,3] Recently, an optical rotator with slopes on its upper surface and a cylindrical body was proposed.[4] The rotator is expected to be aligned with the axis of propagation of the light beam.[5] Because the entire illuminated light beam contributes to the rotation and because the cylindrical shape of the rotor is effective in decreasing the viscous drag force, this new type of rotator is expected to rotate much faster than a conventional rotator.

However, many kinds of complex structure mechanical rotators driven by laser light have been proposed for microelectromechanical systems applications.[6–8] The fields of possible application are micromachining tools,[6] a gear,[8] and a microfluidic control device for the lab on a chip.[9]

We analyze light-driven cylindrical rotators of various slope angles and length-to-radius ratios, for optical torque by using a ray optics model and for drag force by using computational fluid dynamics (CFD), to evaluate the exact rotation characteristics.

2. Analysis of Optical Trapping Force and Optical Torque

Figure 1 shows typical rotators with fundamental shapes driven by optical pressure. Figure 1(a) shows a conventional shuttlecock-type rotator,[1] which has no bilateral symmetry in the horizontal cross section. Optical pressure on the side surface rotates the shuttlecock rotator. Figure 1(b) shows a cylindrical-type rotator,[4] which has slopes on the top, a cylindrical body, and a flat plane on the bottom. The optical pressure on the top surface rotates the cylindrical rotator.

The optical pressure force perpendicular to the surface at an arbitrary point on the top, F, is torsionally directed to the beam axis, as shown in Fig. 2. Force F is decomposed into two components: scattering force F_s, pointing in the direction of the beam axis, and gradient force F_g, pointing in the direction perpendicular to the beam axis. Gradient force F_g (not shown) is decomposed again into torque force F_t and radial force F_r. On the lower surface, only scattering force F_b is exerted, and no z-axis torque is exerted because the surface is perpendicular to the optical axis.

When this research was performed, the authors were with the Faculty of Science and Engineering, Ritsumeikan University, 1-1-1, Nojihigashi, Kusatsu-shi, Shiga, 525 Japan. K. Nagatomi is now with Sanyo Electric Corporation, Anpachi, Gifu 503, Japan. H. Ukita's e-mail address is ukita@se.ritsumei.ac.jp.

Received 10 July 2002; revised manuscript received 17 December 2002.

0003-6935/03/152708-08$15.00/0

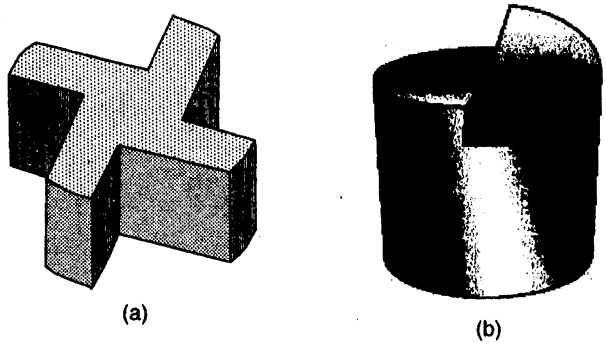

Fig. 1. Fundamental 3D image of shuttlecock (left) and cylindrical (right) types of optical rotator.

A. Illumination by Parallel Beams

We assume that a circularly polarized Gaussian Nd:YAG laser beam (wavelength, $\lambda = 1.064$ μm; power, $P = 100$ mW) illuminates the rotator (refractive index, $n_2 = 1.5$; density, $\rho = 2.2$ g/cm^3; diameter, $2r = 3$ μm; height, $h = 10$ μm) in water ($n_1 = 1.33$). When the rotator is vertically illuminated on the top surface by parallel beams, incident angle a_1 is equal to a (the slope angle of the rotator), and optical pressure F at arbitrary point A is

$$F = [(1 + R)\sin(a) - (n_2/n_1)T \sin(a_2)](n_1P/c) = (n_1PQ/c), \quad (1)$$

where a_2 is the refraction angle, P is the incident power, and Q is the trapping efficiency. Quantities R and T are derived from the Fresnel reflection and transmission coefficients as

$$R = \frac{1}{2}(R_s + R_p) = \frac{1}{2}\left[\frac{\tan^2(a_2 - a_1)}{\tan^2(a_2 + a_1)} + \frac{\sin^2(a_2 - a_1)}{\sin^2(a_2 + a_1)}\right], \quad (2)$$

$$T = 1 - R, \quad (3)$$

where R_s and R_p are the reflectivities for s polarization and p polarization, respectively. Scattering force F_s and torque force F_t at point A are given by

$$F_s = F \cos(a), \quad (4)$$

$$F_t = F_g \sin(\theta) = F \sin(a) \sin(\theta). \quad (5)$$

Therefore torque T_q at the point is

$$T_q = rF_t = (n_1PQ_t/c), \quad (6)$$

where Q_t is the torque efficiency in meters.

When a surface is vertically illuminated by parallel beams, all the refracted light is reflected by the side surface such that the incident angle to the bottom surface is a–a_2. Therefore optical pressure F_b at the bottom surface is given by

$$F_b = [(n_2/n_1)(1 + R')\sin(a - a_2) - T' \sin(a_3)] \times (n_2P'/c), \quad (7)$$

where a_3 is the angle of refraction for incident angle a–a_2. P' is the incident light at the bottom, R' is the reflectivity, and T' is the transmissivity at the bottom. The total trapping force is given the total sum of these:

$$F_{trap} = \iint (F_s + F_b)dS, \quad (8)$$

and the total torque acting on the rotator, M_{opt}, is

$$M_{opt} = \frac{n_1}{c} P \iint Q_t dS. \quad (9)$$

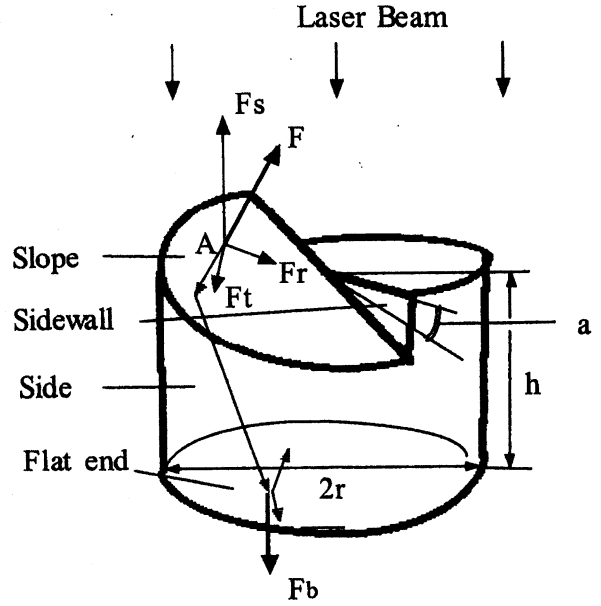

Fig. 2. Rotation relative to the optical pressure exerted on the slopes of the cylindrical rotator.

Figure 3 shows the dependence of the trapping

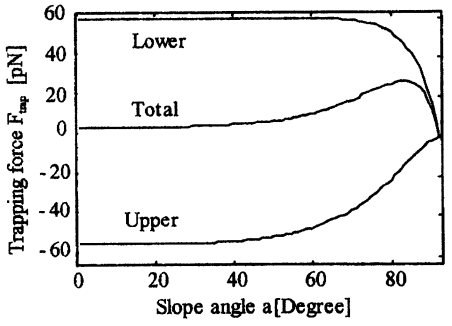

Fig. 3. Dependence of trapping efficiency on slope angle. Incident beam power, $P = 100$ mW; rotator diameter, $2r = 3$ μm; length, $h = 10$ μm.

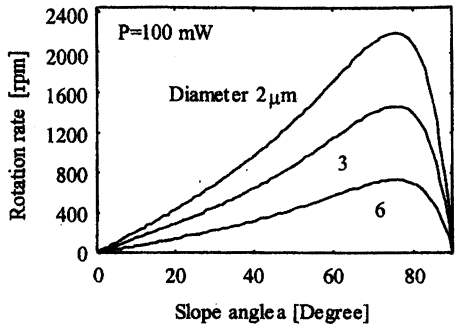

Fig. 4. Dependence of rotation rate on slope angle.

forces on the slope angle. We have defined the positive axial trapping force to be in the $+z$ direction. Pressure is exerted on the top (Upper), bottom (Lower), and both (Total) surfaces. As all the rays refracted on the top surface are reflected from the side surface, scattering force F_b on the flat bottom is always greater than scattering force F_s on the top. Thus the net trapping force $(F_b - F_s)$ pushes the rotator away, which leads to two-dimensional trapping.

Figure 4 shows the dependence of the rotation rate on the slope angle. Assuming that the rotator is cylindrical, we can approximate the rotation speed by $M_{opt} = 4\pi\mu r^2 h\omega$, where M_{opt} is the optical torque of Eq. (9), μ is the medium's viscosity ($\mu = 1$ mPa), r is the radius, h is the length of the rotator, and ω is the angular velocity.

B. Illumination by a Focused Beam

We used a ray tracing method that factors in the beam waist to analyze the optical forces exerted by a focused laser beam. Figure 5 shows the ray tracing for the rotator illuminated by a focused beam. An incident ray repeats reflection and refraction on each surface of the rotator. The minimum radius at the

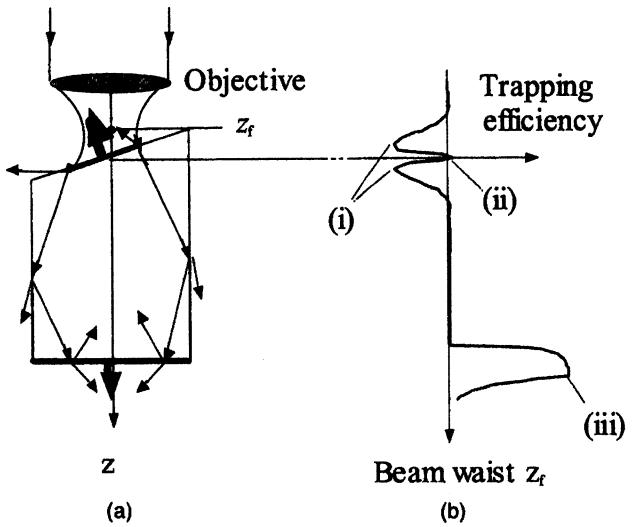

Fig. 5. (a) Ray tracing for the rotator illuminated with a focused beam and (b) trapping efficiency along the light beam's axis.

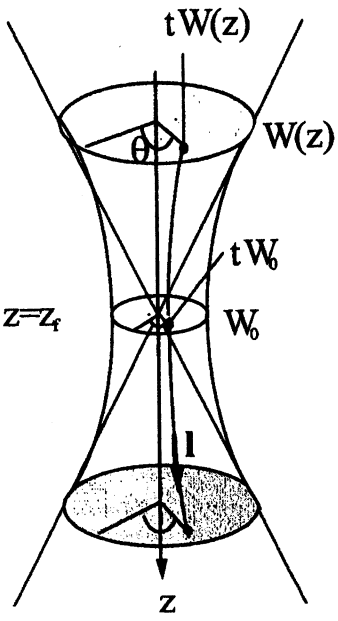

Fig. 6. Ray optics model of a focused laser beam, showing the beam waist. Ray $tW(z)$ passes tW_0 at the beam waist ($z = z_f$), where $0 \le t \le 1$.

waist should be considered in the numerical analysis, especially for the cylindrical rotator, because the rotator's torque, i.e., optical pressure times radius, is exerted on its surface upon which light is incident.

When the rotator is illuminated by a focused laser beam, the individual rays propagate parabolically near the waist, as shown in Fig. 6. The Gaussian beam's radius on the z-directed propagation axis is given by

$$W(z) = W_0\left[1 + \left(\frac{z - z_f}{Z_0}\right)^2\right]^{1/2}, \qquad (10)$$

where W_0 is the minimum waist radius, z_f is the minimum waist position, and $2Z_0$ corresponds to the depth of focus. An arbitrary point on the ray, angle θ in the xy plane, can be described as

$$W(z)\cos\theta, \qquad W(z)\sin\theta, \quad z. \qquad (11)$$

Ray vector $\mathbf{I}$ of $tW(z)$ that passes through $tW_0 (0 \le t \le 1)$ on the beam waist ($z = z_f$) plane can be expressed as

$$I = [tW'(z)\cos\theta, \qquad tW'(z)\sin\theta, z], \qquad (12)$$

where $W'(z)$ is the z derivative of $W(z)$. We can write reflected ray vector $\mathbf{I}_r$ and refracted ray vector $\mathbf{I}_t$ on the incident plane by using vector $\mathbf{I}$ of the incident $tW(z)$ ray as

$$\mathbf{I}_r = \mathbf{I} - 2(\mathbf{I}\cdot\mathbf{n})\mathbf{n}, \qquad (13)$$

$$\mathbf{I}_t = \mathbf{I} + (\mathbf{I}\cdot\mathbf{n})\left[\frac{\tan(a_2)}{\tan(a_1)} - 1\right]\mathbf{n}, \qquad (14)$$

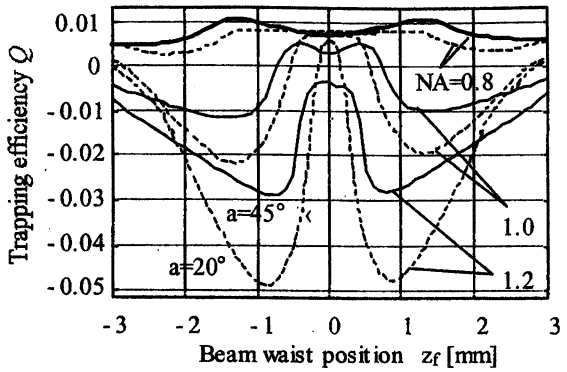

Fig. 7. Dependence of trapping efficiency Q on beam waist position z_f for several NAs and slope angles a, where $P = 100$ mW, $2r = 3$ μm, and $h = 10$ μm.

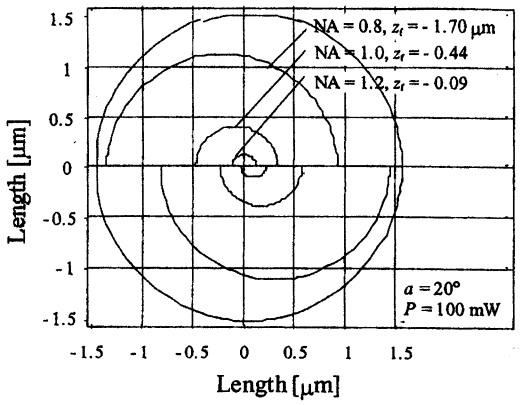

Fig. 9. Top view of a region illuminated by a focused beam for three NAs.

where **n** defines the vector normal to the interface, a_1 is the angle of incidence, and a_2 is the angle of refraction.

We calculated the optical force at each point by these ray vectors as follows: We traced the rays until they hit the bottom surface and computed the optical pressure on each surface. The light reflected from the bottom caused an error in the optical pressure. The ratio of the reflected light to the input light was below 0.3%, and the computation error was negligible. In the computation the beam was divided into 80 × 80 equal-area segments on the aperture.

Figure 7 shows examples of trapping efficiency Q, and Fig. 8 shows torque efficiency Q_t versus beam waist position for slope angles $a = 20°$ and $a = 45°$ with numerical aperture (NA) as a parameter. The negative value of Q is illustrated in Fig. 7. It indicates that the trapping force pulls the rotator toward the focused point of the incident beam, which leads to three-dimensional (3D) trapping. Torque efficiency Q_t increases as NA decreases. Fast rotation is possible when the NA decreases to produce a light beam with a large radius on the top surface.

Figure 9 shows the illuminated region on the upper surface where $a = 20°$ for several NAs, where $P = 100$ mW. The radius of the illuminated region decreases as the NA increases. Therefore the optical torque, i.e., the rotation rate, also decreases as the NA increases. Figure 10 shows the relationship between the rotation rate and beam's intensity for two NAs, assuming that $M_{opt} = 4\pi\mu r^2 h\omega$. The rotation rate is linearly proportional to the beam's intensity, and it increases as NA decreases. A rotation rate as high as 700 rpm is predicted when a 100-mW laser beam with a focused beam illumination of NA = 0.8 is used.

C. Effect of Light-Beam Profiles

The trapping force and the rotation rate are calculated for beam intensity profiles of the following forms:

(a) TEM_{00} (Gaussian) mode $I(r) = I_0 \exp(-2r^2/w_0^2)$,
(b) Uniformly filled aperture mode $I(r) = I_0$,
(c) TEM_{01} (doughnut) mode $I(r) = I_0(r/w_0)^2 \exp(-2r^2/w_0^2)$.

The fractions of the total beam intensity that enter the lens aperture for these profiles are (a) 87%, (b)

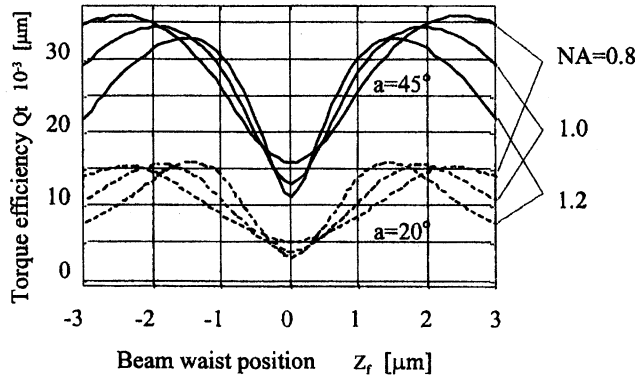

Fig. 8. Relation between torque efficiency Q_t on beam waist position z_f for several NAs and slope angles a.

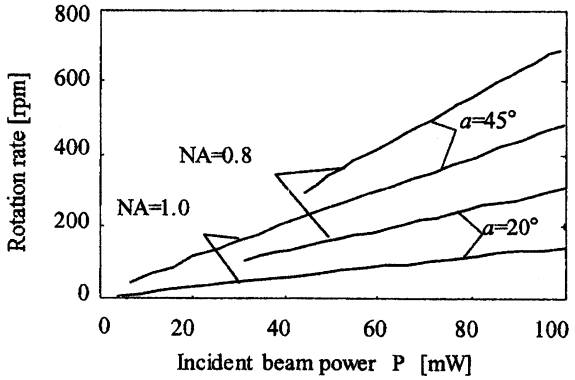

Fig. 10. Relationship between rotation rate and slope angle of a focused beam for the approximation $M_{opt} = 4\pi\mu r^2 h\omega$, where M_{opt} is the optical torque, μ is the medium's viscosity, r is the radius, h is the length of the rotator, and ω is the angular velocity.

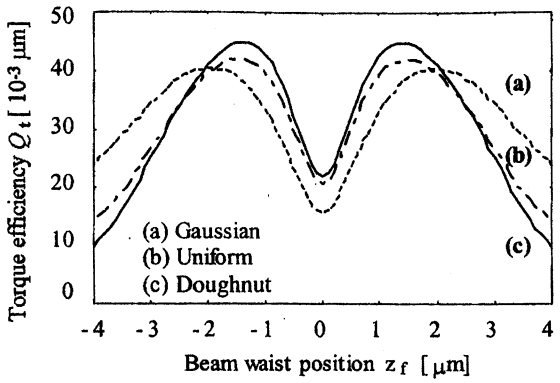

Fig. 11. Relationship between torque efficiency Q_t and beam waist position z_f for several beam profiles.

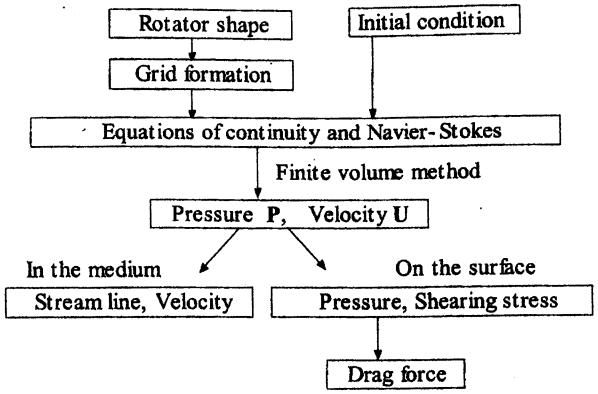

Fig. 13. Flow chart of a drag force analysis by the finite-volume method.

100%, and (c) 59%. Below, all the beam intensities are normalized after the lens aperture.

Figure 11 shows the relation between torque efficiency Q_t and beam waist position z_f for beam profiles (a)–(c). Because the torque at an arbitrary point is defined as the product of force F_t and distance r from the rotation axis, high torque efficiency can be obtained by beam profile (c), which has a strong intensity at the outer part (large r) of the aperture. Good trapping and fast rotation are possible when the outer part of the input aperture is filled by light of strong intensity. Figure 12 shows the dependence of the rotation rate on the incident intensity for two NAs. The rotation rate increases as the intensity of the outer part of the aperture becomes strong. We can improve the rotation rate by using the incident-beam profiles.[10]

3. Analysis of Fluid Characteristics

To evaluate the performance of the optical rotator in water we investigated the viscous drag force acting on the surface of the rotator and the stream lines about the rotator, using a fluid flow solver (computational fluid dynamics).[11]

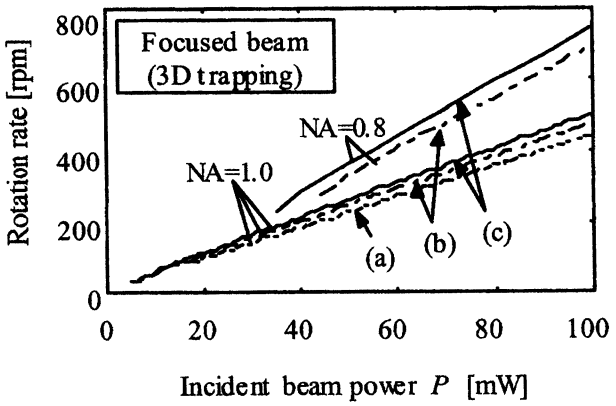

Fig. 12. Relationship between rotation rate and focused beam power for several profiles; diameter $2r = 3$ μm and height $h = 10$ μm.

A. Computational Fluid Dynamics

Continuity equation (15) and Navier–Stokes equation (16) are

$$\nabla \cdot (\mathbf{U} - \mathbf{u}) = 0, \tag{15}$$

$$\frac{\partial \mathbf{U}}{\partial t} + [(\mathbf{U} - \mathbf{u}) \cdot \nabla]\mathbf{U} = -\nabla P + \nu \nabla^2 \mathbf{U}, \tag{16}$$

where $\mathbf{U}$ is the fluid velocity, $\mathbf{u}$ is the velocity of the sliding mesh, t is the time, P is the pressure, and ν is the kinematic viscosity. The simulation was performed in a 3D geometry with a commercial computational fluid dynamics tool (CFX-4, AEA Corporation). The control volume was a cube, and each domain had a set of discretized equations that we formulated by evaluating and integrating the fluxes across the faces of the volume to satisfy the equations. Figure 13 shows the simulation procedure. To discretize Eqs. (15) and (16) we used the finite-volume method. We ran through a number of iterations, trying to minimize the overall change in selected parameters from one iteration to another. If the error was below a prescribed value, the iteration was terminated. Otherwise, we continued the iteration and obtained pressure P and velocity $\mathbf{U}$ for each volume.

The velocity vectors (Fig. 14) and the stream lines (Fig. 15) in the proximity of the rotator at a speed of 3000 rpm were analyzed for the rotator described above (refractive index, $n_2 = 1.5$; diameter, $2r = 3$ μm; height, $h = 10$ μm; slope angle, $\alpha = 45°$). The fluid is water ($n_1 = 1.33$) at 283 K (incompressible viscous flows; density, $\rho = 1.0$ g/cm^3; viscosity, $\mu = 1.328 \times 10^{-3}$ Pa). The corresponding Reynolds number ($\mathrm{Re} = r\omega d^2/4\pi$) is 10^{-4} at 3000 rpm.

Figure 14 shows that the velocity increases close to the rotator and the flow goes upward near one part of the top (A) but downward near the opposite part of the top (B) in counterclockwise rotation. The streamline of Fig. 15 shows that the flow goes outward and upward in the proximity of the slope.

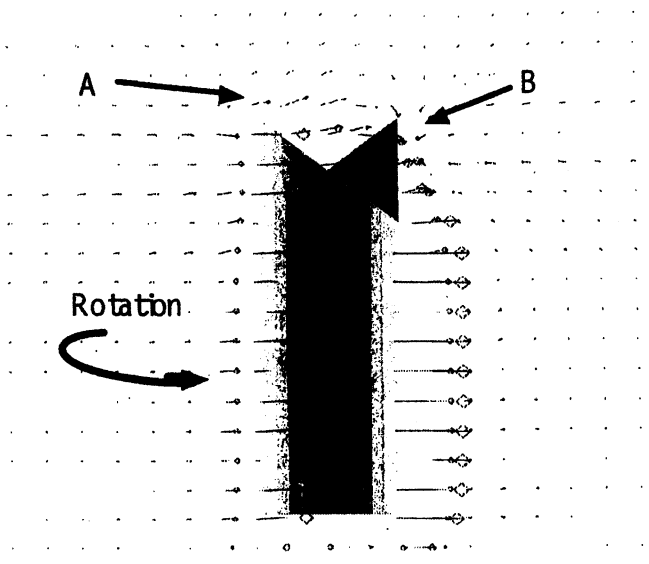

. 14. Velocity vectors in the plane at 0.5 μm before the center plane for an optical rotator: $a = 45°$, $2r = 3$ μm, $h = 10$ μm.

B. Pressure and Shearing Stress

Figure 16 shows pressure P and shearing stress S ($=dU/dx$) on the surface of the rotator. Large pressure (1.24 pN/μm^2) appears on the upper edge of the slope where the fluid velocity is high. Flow-in occurs near the sidewall as a result of the negative pressure. The pressure on the flat end is small because of the tangential direction of the rotation axes. The shearing stresses, however, are large on the top of the edge (2.24 pN/μm^2). The shearing stress on the side surface is small, which leads to a small fluid flow along the side surface.

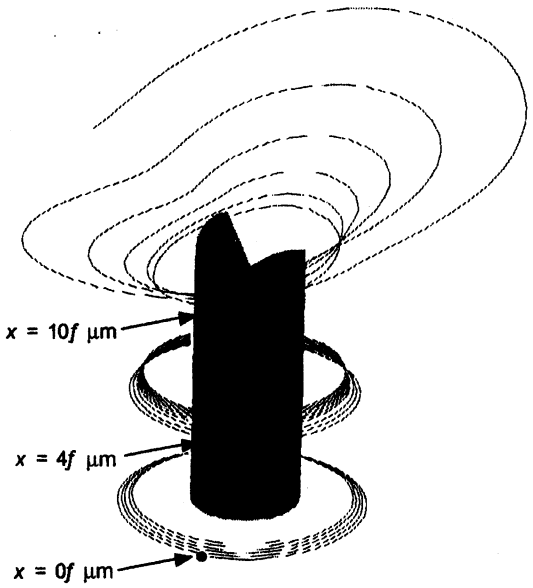

Fig. 15. Streamlines about the rotator.

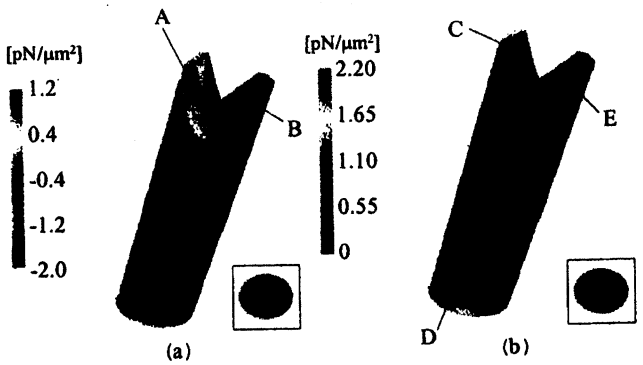

Fig. 16. 3D images of (a) the pressure distribution and (b) the shearing stress distribution.

C. Viscous Drag Force

Viscous drag force M_{drag} acting on the surface of the rotator is evaluated as follows: Drag forces that are due to the pressure (normal component) and to the shearing stress (tangential component) on all the surfaces are integrated as

$$M_{drag} = \iint r^2(P_t + S_t)\mathrm{d}r\mathrm{d}\theta, \qquad (17)$$

where P_t is the torque component of pressure P, S_t is that of the shearing stress, and r is the radius at that point. The parameters used for the analysis are slope angle a and cylinder length h of a rotator with a 3-μm diameter.

Table 1 shows a comparison of the drag force between the CFD [computed with Eq. (17)] and the approximation methods for 3000-rpm optical rotators with $a = 45°$, $2r = 3$ μm, and $h = 3$ μm. The sum of the drag forces on the slope (6.37 pN/μm^2) and on the sidewall (4.99 pN/μm^2) is three times that of the flat end (3.56 pNμm). Table 2 lists the drag force of each part of the rotator simulated by the CFD method. Figure 17 shows the dependence of the drag force on the rotator length for a comparison of the CFD and the approximation methods. It is clear that, as the rotator length decreases, the drag force difference between the CFD and the approximation methods increases, as expected.

Table 1. Comparison of Drag Force of 3000-rpm Optical Rotators for $a = 45°$, $2r = 3$ μm, and $h = 3$ μm

	Method (pNμm)	
Parts of Rotors	CFD	Approximation[a]
Slopes	6.37	0
Sidewalls	4.99	0
Side	39.3	35.4
Flat End	3.56	0
Total	54.2	35.4

[a] $4\pi\mu r^2 h\omega$.

Table 2. Drag Forces of Surfaces on a 3000-rpm Optical Rotator Simulated by CFD for $2r = 3$ μm and $h = 3$ μm

Parts of Surfaces Subjected to Drag Forces (in pNμm)	Slope Angle		
	0°	30°	60°
Slopes	3.60	5.07	8.10
Sidewalls	0	3.07	9.27
Side	43.7	38.2	41.5
Flat end	3.60	3.56	3.61
Total	48.1	49.9	62.5

4. Rotation Characteristics

We adjust the rotation rate by balancing optical torque M_{opt} of Eq. (9) with drag force M_{drag} of Eq. (17). Figure 18 compares rotation rates for the CFD and the approximation methods for an $\alpha = 45°$ rotator with the rotator length as a parameter. Figure 19 compares the rotation rates for the CFD and the approximation methods with the slope angle as a parameter. A laser power of 100 mW is directed onto the rotator by parallel-beam illumination.

From these figures we confirmed that the slope effect on the drag force becomes clear for lengths smaller than 10 μm or for a slope angle greater than 30°. The rotation rates for CFD for a rotator with a 3-μm diameter and a 3-μm length are 0.67 (slope angle, $\alpha = 45°$) and 0.56 ($\alpha = 60°$) times the approximation value.

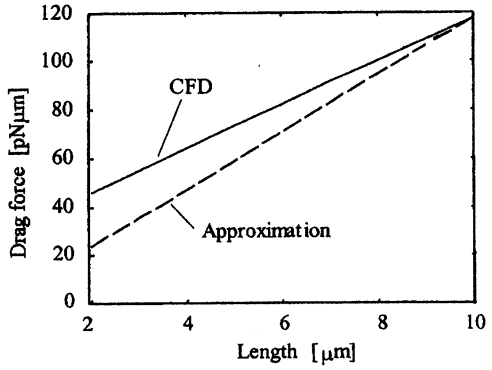

Fig. 17. Comparison of drag force in the CFD and approximation method with rotator length as a parameter.

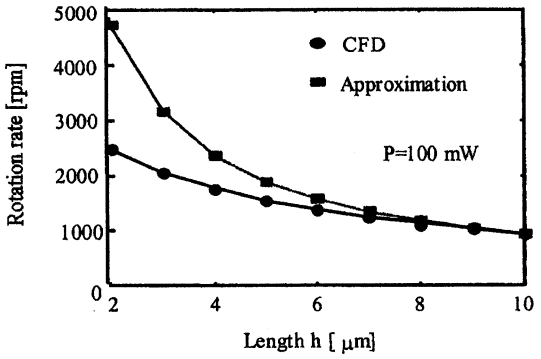

Fig. 18. Comparison of rotation rates for CFD and approximation methods with parallel beam illumination for $\alpha = 45°$, $2r = 3$ μm, and $h = 10$ μm with rotator length as a parameter.

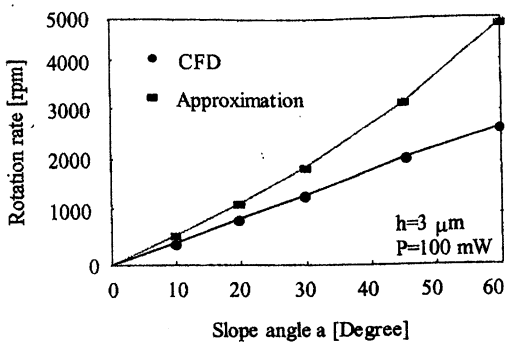

Fig. 19. Comparison of rotation rates for the CFD and the approximation methods, with slope angle as a parameter.

5. Conclusions

We have described a cylindrical optical rotator with slopes on its upper surface. The rotator is held and rotated by laser tweezers. Its optical torque and viscous drag force were analyzed with a ray optics model and by computational fluid dynamics. We evaluated the rotation rate by balancing the optical torque with the drag force.

First, the total optical torque M_{opt} acting on the rotator was given as the sum of the torque that was due to the optical pressure on all the incident surfaces (slopes) of the rotator for both parallel and focused beam illumination, with the slope angle and the rotator length and diameter as parameters. Second, we analyzed viscous drag force M_{drag} acting on the surface of the rotator by using the CFD, integrating the pressure and the shearing stress on all the surfaces of the rotator.

As a result, the slope effect on the drag force became clear for a slope angle greater than 30° and lengths less than 10 μm. The rotation rates obtained with the ray optics model and CFD for a rotator with a 3-μm diameter and 3-μm length are 0.67 (slope angle, 45°) and 0.56 (60°) times the approximation value by the ray optics model for a cylindrical body drag force of $4\pi\mu r^2 h\omega$.

A comparison has also been given for the performance of the rotator when different beam intensity profiles are used. The results confirmed that the optical pressure rotation rate is improved when a doughnut-shaped beam is used because the dominant intensity of the beam's outer part is effective in producing torque on the incident surface.

The authors thank Y. Ogami and K. Nagumo of Ritsumeikan University for their help with the computational fluid dynamics.

References

1. E. Higurashi, H. Ukita, H. Tanaka, and O. Ohguchi, "Optically induced rotation of micro-objects fabricated by surface micromachining," Appl. Phys. Lett. **64**, 2209–2210 (1994).
2. R. C. Gauthier, "Ray optics model and numerical computation

for the radiation pressure micromotor," Appl. Phys. Lett. **67,** 2269–2271 (1995).
3. Y. Ohmachi, K. Baba, and E. Higurashi, "Numerical analysis of an optical motor based on the radiation pressure," in *Micromachined Devices and Components II*, K. Chao and M. Roop, eds., Proc. SPIE **2882,** 333–338 (1996).
4. H. Ukita and K. Nagatomi, "Theoretical demonstration of a micro-rotator driven by optical pressure on the light incident surface," Opt. Rev. **4,** 447–449 (1997).
5. R. C. Gauthier, "Theoretical investigation of the optical trapping force and torque on cylindrical micro-objects," J. Opt. Soc. Am. B **14,** 3323–3333 (1997).
6. P. Galajda and P. Ormos, "Complex micromachines produced and driven by light," Appl. Phys. Lett. **78,** 249–251 (2001).
7. M. E. J. Friese and H. Rubinsztein-Dunlop, "Optically driven micromachine elements," Appl. Phys. Lett. **78,** 547–549 (2001).
8. S. Maruo, K. Ikuta, and K. Hayato, "Light-driven MEMS made by high-speed two-photon microstereolithography," presented at the Meeting on Micro Electro Mechanical Systems, Interlaken, Switzerland, 21–25 January, 2001.
9. H. Ukita and M. Kanehira, "A shuttlecock optical rotator—its design, fabrication and evaluation for a micro-fluidic mixer," IEEE J. Sel. Top. Quantum Electron. **8,** 111–117 (2002).
10. K. Nagatomi and H. Ukita, "Improvement in optical rotation rate of a cylindrical micro-objects by incident beam profiles," presented at the Conference on Optical MEMS and Their Applications (MOEMS '97), Nara, Japan, 18–21 November 1997.
11. K. Nagumo, Y. Ogami, K. Nagatomi, and H. Ukita, "Investigation on mixing performance by a shuttlecock optical microrotor," presented at the 8th International Symposium on Transport Phenomena and Dynamics of Rotating Machinery, ISROMAC-8, Honolulu, Hawaii, 26–30 March 2000.